Microstructural effects on the permeability of periodic fibrous porous media

K. Yazdchi, S. Srivastava and S. Luding

Multi Scale Mechanics (MSM), Faculty of Engineering Technology,
University of Twente, P.O. Box 217, 7500 AE Enschede, The Netherlands

Abstract

An analytical-numerical approach is presented for computing the macroscopic permeability of fibrous porous media taking into account their micro-structure. A finite element (FE) based model for viscous, incompressible flow through a regular array of cylinders/fibers is employed for predicting the permeability associated with this type of media. High resolution data, obtained from our simulations, are utilized for validating the commonly used semi-analytical models of drag relations from which the permeability is often derived. The effect of porosity, i.e., volume fraction, on the macroscopic permeability is studied. Also micro-structure parameters like particle shape, orientation and unit cell staggered angle are varied. The results are compared with the Carman-Kozeny (CK) equation and the Kozeny factor (often assumed to be constant) dependence on the micro-structural parameters is reported and used as an attempt to predict a closed form relation for the permeability in a variety of structures, shapes and wide range of porosities.

Keywords: Permeability; Fibrous porous media; FEM; Drag relations; Carman-Kozeny equation; Incompressible fluids.

1. Introduction

The problem of creeping flow between solid bodies arranged in a regular array is fundamental in the prediction of seepage through porous media and has many applications, including: composite materials (Dullien 1992, Laakkonen 2003), rheology (Muller et al. 1999, Moss et al. 2010), geophysics (Berryman et al. 2000), polymer flow through rocks (Sorbie et al. 1987), statistical physics (Hilfer 2000, Chen et al. 2008), colloid science (Shani et al. 2008), soil science (Roth 2008, Crawford et al. 1995) and biotechnology (Wanner et al. 1995). A compelling motivation for such studies concerns the understanding, and eventually the prediction, of single and multiphase transport properties of the pore structure.

A specific category of porous media is formed by 2D long cylinders or fiber-like particles. Restricted flow through fibrous porous materials has applications in several engineering/industrial areas including: filtration and separation of particles, composite fabrication, heat exchangers, thermal insulations, etc. Prediction of the hydraulic permeability of such materials has been vastly studied in the past decades. It is known that, for fiber reinforced composites, the microstructure of the reinforcement strongly influences the permeability. This study presents an interesting step towards a unified understanding of the effect of microstructure (e.g. particle/fiber shape and orientation) on the macroscopic permeability by combining numerical simulations with analytical prediction in a wide range of porosity.

Usually, when treating the medium as a continuum, satisfactory predictions can be obtained by Darcy's law, which lumps all complex interactions between the fluid and fibers/particles into K, the permeability (tensor). Accurate permeability data, therefore, is a critical requirement for macroscopic simulations based on Darcy's law – to be successfully used for design and optimization of industrial processes.

The Ergun equation is a semi-empirical drag relation from which the permeability of porous media can be deduced. It is obtained by the direct superposition of two asymptotic solutions, one for very low Reynolds number, the Carman-Kozeny (CK) equation (Bird et al. 2001), and the other for very high Reynolds numbers, the Forchheimer correction (Bird et al. 2001). However, these approximations do not take into account the micro-

structural effects, namely the shapes and orientations of the particles, such that not only local field properties but also some global properties (such as anisotropy) cannot be addressed.

In this respect, two distinct approaches seem to have emerged. The first approach is based on lubrication theory and considers the pores of a porous medium as a bunch of capillary tubes which are tortuous or interconnected in a network (Bird et al. 2001). Even though this model has been used successfully for isotropic porous media, it does not work well for either axial or transverse permeability of aligned fibrous media (Bruschke et al. 1993).

The second approach (cell method) considers the solid matrix as a cluster of immobile solid obstacles, which collectively contribute Stokes resistance to the flow. For a review of these theories see Dullien 1992 and Bird et al. 2001. When the solids are dilute, i.e., at high porosities, basically the particles do not feel each other, so that cell approach is appropriate. Bruschke and Advani (1993) used lubrication theory in the high fiber volume fraction range but adopted an analytical cell model for lower fiber volume fractions. A closed form solution, over the full fiber volume fraction range, is obtained by matching both solutions asymptotically.

Prediction of the permeability of fibrous media dates back to experimental work of Sullivan (1942) and theoretical works of Kuwabara (1959), Hasimoto (1959), and Happel (1959). The parallel flow solutions are idealized solutions for the flow through cigarette filters, plant stems and around pipes in heat exchange tanks. The transverse solutions are applicable to transverse fibrous filters used for cleaning liquids and gases and regulating their flow. Both types of solutions can also be applicable to the settling of suspensions of long thin particles. A comprehensive review of experimental works of permeability calculation of these systems is available in Jackson et al. (1986) and Astrom et al. (1992).

Later, Sangani and Acrivos (1982), performed analytical and numerical studies of the viscous permeability of square and staggered arrays of cylinders. Their analytical models were accurate in the limits of low and high porosity. For high densities they obtained the lubrication type approximations for narrow gaps. Drummond and Tahir (1984) modeled the flow around a fiber using a unit cell approach (by assuming that all fibers in a fibrous medium experience the same flow field) and obtained equations that are applicable at

lower volume fractions. Gebart (1992) presented an expression for the longitudinal flow, valid at high volume fractions, that has the same form as the well-known KC equation. For transverse flow, he also used the lubrication approximation, assuming that the narrow gaps between adjacent cylinders dominate the flow resistance. Using the Eigen-function expansions and point match methods, Wang (2002) studied the creeping flow past a hexagonal array of parallel cylinders.

Our literature survey indicates that relatively little attention has been paid to the macroscopic permeability of ordered periodic fibrous materials. More importantly, the majority of the existing correlations for permeability are based on curve-fitting of experimental or numerical data and most of the analytical models found in the literature are not general and fail to predict permeability over the wide range of porosity, since they contain some serious assumptions that limit their range of applicability.

In this study, periodic arrays of parallel cylinders (with circular, ellipse and square cross-section) perpendicular to the flow direction are considered and studied with a FE based model in section 2. The effects of shape and orientation as well as porosity and structure on the macroscopic permeability of the porous media are discussed in detail. In order to relate our results to available work, the data are compared with previous theoretical and numerical data for square and hexagonal packing configurations and a closed form relation is proposed in section 3 in the attempt to combine our various simulations. The paper is concluded in section 4 with a summary and outlook for future work.

2. Results from FE simulations

This section is dedicated to the FE based model simulations and the results on permeability as function of porosity, structure, shape and anisotropy.

2.0. Introduction and Terminology

The superficial velocity, *U*, within the porous media in the unit cell is defined as

$$U = \frac{1}{V}\int_{V_f} u dv = \varepsilon \langle u \rangle \quad , \tag{1}$$

where u, $\langle u \rangle$, V, V_f and ε are the local microscopic velocity of the fluid, corresponding averaged velocity, total volume, volume of the fluid and porosity, respectively. For the case where the fluid velocity is sufficiently small (creeping flow), the well-known Darcy's law relates the superficial fluid velocity U through the pores with the pressure gradient, ∇p, measured across the system length, L, so that

$$U = -\frac{K}{\mu}\nabla p \quad , \tag{2}$$

where μ and K are the viscosity of the fluid and the permeability of the sample, respectively. At low Reynolds numbers, which are relevant for most of the composite manufacturing methods, the permeability depends only on the geometry of the pore structure. By increasing the pressure gradient, we observed a typical departure from Darcy's law (creeping flow) at sufficiently high Reynolds number, Re>0.1 (data not shown here). In order to correctly capture the influence of the inertial term, Yazdchi et al. (2010) showed that the original Darcy's Law can be extended with a power law correction with powers between 2 and 3 for square or hexagonal configurations. Hill et al. (2001) examined the effect of fluid inertia in cubic, face-centered cubic and random arrays of spheres by means of lattice-Boltzmann simulations. They found good agreement between the simulations and Ergun correlation at solid volume fractions approaching the closely-packed limit at moderate Reynolds number (Re<100).

Recently, models based on Lagrangian tracking of particles combined with computational fluid dynamics for the continuous phase, i.e., discrete particle methods (DPM), have become state-of-the-art for simulating gas-solid flows, especially in fluidization processes (see e.g. Kuipers et al. 1993). In this method, two-way coupling is achieved via the momentum sink/source term, S_p which models the fluid-particle drag force

$$S_p = \beta\left(\langle u \rangle - v_p\right), \tag{3}$$

where the interphase momentum-transfer coefficient, β, describes the drag of the gas/fluid phase acting on the particles and v_p is the velocity of particles. (Additional effects like the added mass contributions are disregarded here for the sake of simplicity.) In steady state, without acceleration, wall friction, or body forces like gravity, the fluid momentum balance reduces to

$$-\varepsilon\nabla p-\beta\left(\langle u\rangle-v_p\right)=0\,. \tag{4}$$

By comparing Eqs. (2) and (4), using the definition of Eq. (1), and assuming immobile particles, i.e., $v_p=0$, the relation between β and permeability *K* is

$$\beta=\frac{\mu\varepsilon^2}{K}\quad. \tag{5}$$

Accurate permeability data, therefore, is a critical requirement in simulations based on DPM to be successfully used in the design and optimization of industrial processes.

In the following, results on the permeability of two-dimensional (2D) regular periodic arrays of cylinders with different cross section are obtained by incorporating detailed FE simulations. This is part of a multiscale modeling approach and will be very useful to generate closure or coupling models required in more coarse-grained, large-scale models.

2.1. Mathematical formulation and boundary conditions

Both hexagonal and square arrays of parallel cylinders perpendicular to the flow direction are considered, as shown in Fig. 1. The basis of such model systems lies on the assumption that the porous media can be divided into representative volume elements (RVE) or unit cells. The permeability is then determined by modeling the flow through one of these, more or less, idealized cells. FEM software (ANSYS) is used to calculate the superficial velocity and, using Eq. (2), the permeability of the fibrous material. A segregated, sequential solution algorithm is used to solve the steady state Navier-Stokes (NS) equations combined with the continuity equation. In this approach, the momentum equations (i.e. NS equations) are used to generate an expression for the velocity in terms of the pressure gradient. This is used in the continuity equation after it has been integrated by parts. This nonlinear solution procedure belongs to a general class of the Semi-Implicit Methods for Pressure Linked Equations (SIMPLE). The developed matrices from assembly of linear triangular elements are solved based on a Gaussian elimination algorithm. It is robust and can be used for symmetric as well as non-symmetric equation systems but requires extensive computational memory already in 2D. At the left and right pressure- and at the top and bottom periodic-boundary conditions are applied. The no-slip boundary condition is applied on the surface of the particles/fibers. A typical unstructured, fine and triangular FE mesh is also shown in Fig. 1(c). The mesh

size effect is examined by comparing the simulation results for different resolutions (data are not shown here). The range of number of elements is varying from 10^3 to 10^4 depending on the porosity regime. It should be noted that in Darcy's linear regime (creeping flow) – although we have applied pressure boundary conditions at left and right – identical velocity profile at inlet and outlet are observed, due to the symmetry of this geometry and linearity. However, by increasing the pressure gradient (data not shown), the flow regime changes to non-linear and becomes non-symmetric. Furthermore, because of the symmetry in the geometry and boundary conditions, the periodic boundary condition and symmetry boundary condition, i.e., zero velocity in vertical direction at top and bottom of the unit cells, will lead to identical results (as confirmed by simulations – data not shown).

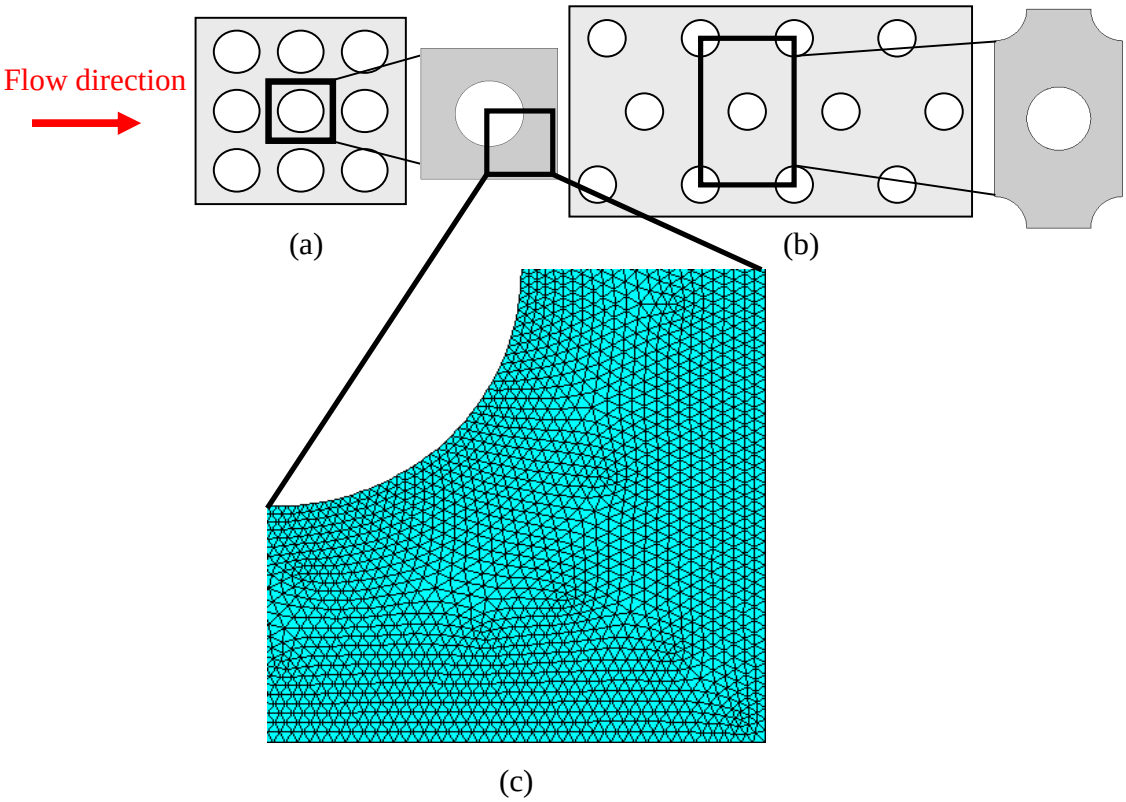

Figure 1: The geometry of the unit cells used for (a) square and (b) hexagonal configurations, with angles 45^0 and 60^0 between the diagonal of the unit-cell and the

horizontal flow direction (red arrow), respectively. (c) shows a typical quarter of an unstructured, fine and triangular FE mesh.

2.2. Permeability of the square and hexagonal arrays

Under laminar, steady state condition, with given viscosity, the flow through porous media is approximated by Darcy's law. By calculating the superficial velocity, U, from our FE simulations and knowing the pressure gradient, ∇p, over the length of the unit cell, L, we can calculate the dimensionless permeability (normalized by the cylinder diameter, d), K/d^2. In Table 1, various correlations from the literature are listed. The first relation by Gebart (1992) has a peculiar analytical form and is valid in the limit of high density, i.e., low porosity – close to the close packing limit ε_c (the same as Bruschke et al. (1993) in the low porosity limit, with maximum discrepancy less than 1%). Note that the relations by Happel (1959), Drummond et al. (1984), Kuwabara (1959), Hasimoto (1959), and Sangani et al. (1982) are all identical in their first term – that is not dependent on the structure – in the limit of small solid volume fraction ϕ, i.e., large porosity. In contrast, their second term is weakly dependent on the structure (square or hexagonal). Bruschke et al. (1993) proposed relations that are already different in their first term. The last two relations in the table are only valid in intermediate porosity regimes and do not agree with any of the above relations in either of the limit cases.

In Fig. 2, the variation of the (normalized) permeability, K/d^2, with porosity, for square and hexagonal packings is shown. The lubrication theory presented by Gebart (1992) agrees well with our numerical results at low porosities ($\varepsilon \ll 0.6$), whereas, at high porosities ($\varepsilon \gg 0.6$), the prediction by Drummond et al. (1984) better fits our data. Drummond et al. (1984) have found the solution for the Stokes equations of motion for a viscous fluid flowing in parallel or perpendicular to the array of cylinders by matching a solution outside one cylinder to a sum of solutions with equal singularities inside every cylinder of an infinite array. This was in good agreement with other available approximate solutions, like the results of Kuwabara (1959) and Sangani et al. (1982) at high porosities, as also confirmed by our numerical results (data not shown). Note that

our proposed merging function in section 3.4, fits to our FE results within 2% error for the whole range of porosity.

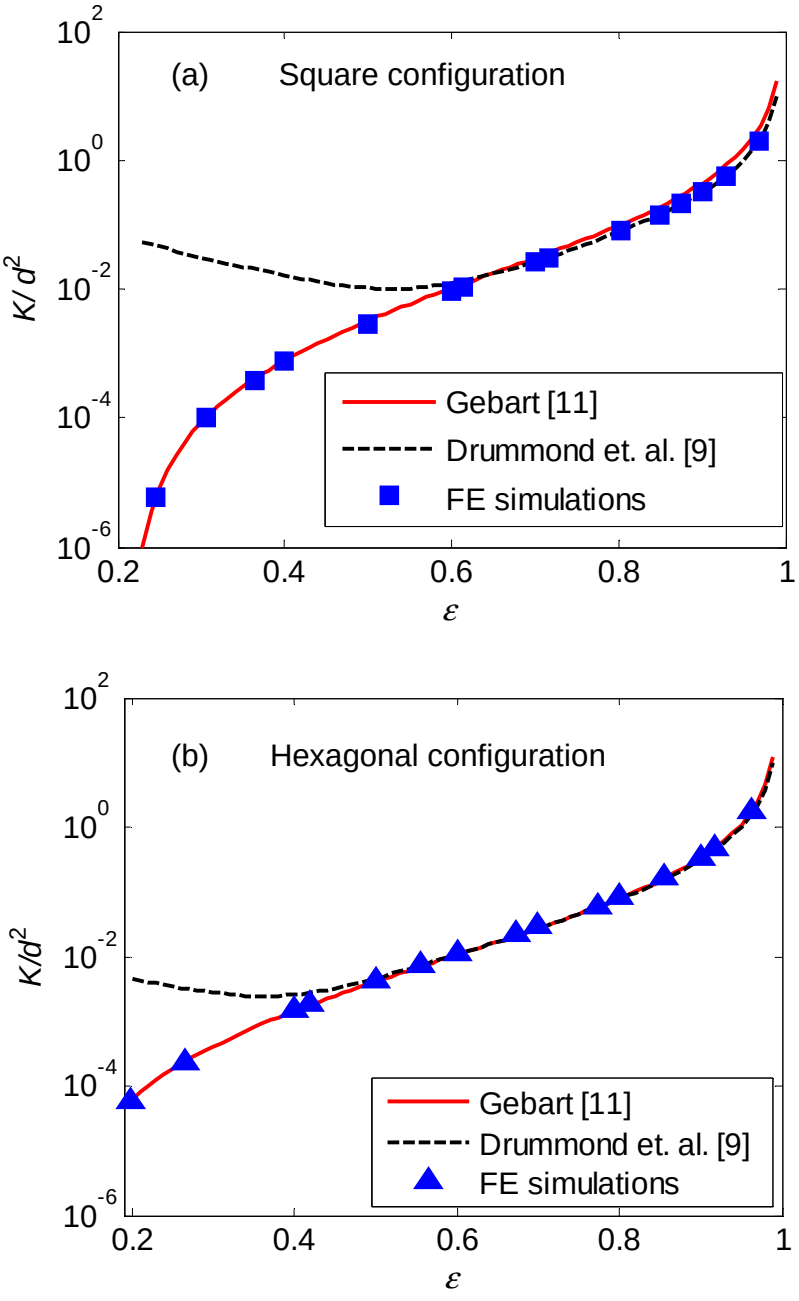

Figure 2: Normalized permeability plotted against porosity for (a) square and (b) hexagonal packing for circular shaped particles/cylinders with diameter d, for perpendicular flow. The lines give the theoretical predictions, see inset. For high porosities, the difference between Gebart (1992) and Drummond et al. (1984), in the

hexagonal configuration, is less than 5%, while for the square configuration it is less than 30%.

Table 1: Summary of correlations between normalized permeability, K/d^2 and porosity, with $\phi = 1-\varepsilon$, the solid volume fraction.

Author	K/d^2	Comments
Gebart (1992)	$C\left(\sqrt{\frac{1-\varepsilon_c}{1-\varepsilon}}-1\right)^{5/2}$ $\left\{\begin{array}{l} C=\frac{4}{9\pi\sqrt{2}},\ \varepsilon_c=1-\pi/4 \\ C=\frac{4}{9\pi\sqrt{6}},\ \varepsilon_c=1-\pi/\left(2\sqrt{3}\right) \end{array}\right\}$	Square configuration: K_G^s/d^2 Hexagonal config.: K_G^h/d^2
Bruschke et al. (1993)	$\frac{\left(1-l^2\right)^2}{12l^3}\left(3l\frac{\tan^{-1}\left(\sqrt{\frac{1+l}{1-l}}\right)}{\sqrt{1-l^2}}+\frac{l^2}{2}+1\right)^{-1}$	Lubrication theory, square config.: $l^2=\frac{4}{\pi}(1-\varepsilon)$
Drummond et al. (1984)	$\frac{1}{32\phi}\left(\ln\left(\frac{1}{\phi}\right)-1.476+\frac{2\phi-0.796\phi^2}{1+0.489\phi-1.605\phi^2}\right)$ $\frac{1}{32\phi}\left(\ln\left(\frac{1}{\phi}\right)-1.497+2\phi-\frac{\phi^2}{2}-0.739\phi^4+\frac{2.534\phi^5}{1+1.2758\phi}\right)$	Square configuration: K_D^s/d^2 Hexagonal config.: K_D^h/d^2
Bruschke et al. (1993)	$\frac{1}{32\phi^2}\left(\ln\left(\frac{1}{\phi}\right)-\frac{3}{2}+2\phi-\frac{\phi^2}{2}\right)$	Cell method, square config.
Kuwabara (1959)	$\frac{1}{32\phi}\left(\ln\left(\frac{1}{\phi}\right)-1.5+2\phi-\frac{\phi^2}{2}\right)$	Based on Stokes approximation
Hasimoto (1959)	$\frac{1}{32\phi}\left(\ln\left(\frac{1}{\phi}\right)-1.476\right)$ Using elliptic functions: $\frac{1}{32\phi}\left(\ln\left(\frac{1}{\phi}\right)-1.476+2\phi+O\left(\phi^2\right)\right)$	----------
Sangani et al. (1982)	$\frac{1}{32\phi}\left(\ln\left(\frac{1}{\phi}\right)-1.476+2\phi-1.774\phi^2+4.076\phi^3\right)$	----------
Happel (1959)	$\frac{1}{32\phi}\left(\ln\left(\frac{1}{\phi}\right)-\frac{1-\phi^2}{1+\phi^2}\right)$	----------
Lee and Yang (1997)	$\frac{\varepsilon^3\left(\varepsilon-0.2146\right)}{31\left(1-\varepsilon\right)^{1.3}}$	Valid for $0.435<\varepsilon<0.937$
Sahraoui et al. (1992)	$\frac{0.0152\pi\varepsilon^{5.1}}{1-\varepsilon}$	Valid for $0.4<\varepsilon<0.8$

2.3. Effect of shape on the permeability of regular arrays

In this subsection, we investigate the anisotropic behavior of permeability due to particle shape in square configuration. Using elementary algebraic functions, Zhao et al. (2006a) derived the analytical solutions for pore-fluid flow around an inhomogeneous elliptical fault in an elliptical coordinate system. Obdam and Veling (1987) employed the complex variable function approach to derive the analytical solutions for the pore-fluid flow within an elliptical inhomogeneity in a two-dimensional full plane. Zimmerman (1996) extended their solutions to a more complicated situation, where a randomly oriented distribution of such inhomogeneous ellipses was taken into account. Wallstrom et al. (2002) later applied the two-dimensional potential solution from an electrostatic problem to solve a steady-state pore-fluid flow problem around an inhomogeneous ellipse using a special elliptical coordinate system. More recently, Zhao et al. (2008) used inverse mapping to transform those solutions into a conventional Cartesian coordinate system.

Here, in order to be able to compare different shapes and orientations, the permeability will be normalized with respect to the obstacle length, L_p, which is defined as

$$L_p = 4 \text{ area / circumference}$$

$$L_p = 2r = d \text{ (for circle)}, \quad L_p = c \text{ (for square)}, \quad L_p = 4\pi ab / A_L \text{ (for ellipse)} \tag{6}$$

where r, c, a and b are the radius of the circle, the side-length of the square, the major (horizontal) and minor (vertical) length of the ellipse, respectively. A_L is the circumference of the ellipse.

By applying the same procedure as in the previous section, the normalized permeability (with respect to obstacle length, L_p) is calculated for different shapes on a square configuration.

In Fig. 3 the normalized permeability is shown as function of porosity for different shapes. At high porosities the shape of particles does not affect much the normalized permeability, but at low porosities the effect is more pronounced. We observe that circles have the lowest and horizontal ellipses the highest normalized permeability.

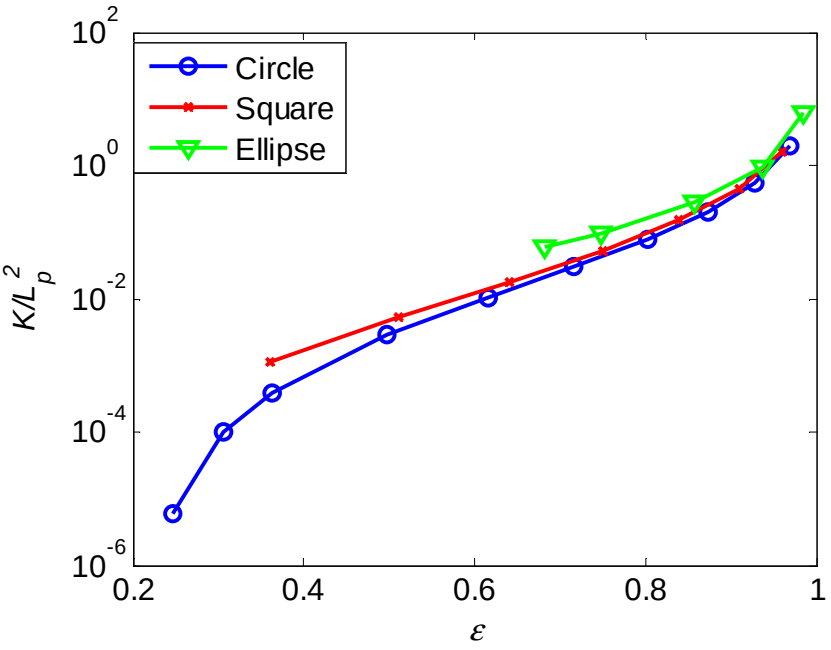

Figure 3: Effect of shape on the normalized permeability from a square packing configuration of circles, squares and ellipses (a/b=2, major axis in flow direction). The lines are only connecting the data-points as a guide to the eye.

2.4. Effect of aspect ratio on the permeability of regular arrays of ellipses

In this subsection the effect of aspect ratio, a/b on the normalized permeability of square-arrays of ellipses is investigated. In fact, the case of high aspect ratio at high porosity represents the flow between parallel plates (slab flow). The relation between average velocity, $\langle u \rangle$, and pressure drop for slab flow is

$$\langle u \rangle = -\frac{h_s^2}{12\mu}\frac{\Delta p}{L} \tag{7}$$

where h_s is the distance between parallel plates (in our square configuration, in the limit $a/b \gg 1$, one has h_s=L=1). Note that, since there are no particles, $\varepsilon = 1$, the average and superficial velocities are identical, i.e., $\langle u \rangle = U$. By comparing Eqs. (7) and (2) the permeability, i.e., $K = h_s^2/12$ is obtained, which indeed shows the resistance due to no slip boundaries at the walls. The variation of permeability for a wide range of aspect ratios at different porosities is shown in Fig. 4. It is observed (especially at high

porosities) that by increasing the aspect ratio the permeability increases until it reaches the limit case of slab flow for which the permeability is $K = h_s^2/12 = 0.0833$ [m^2]. The aspect ratio b/a <1 means that the ellipse stands vertically and therefore the permeability reduces drastically.

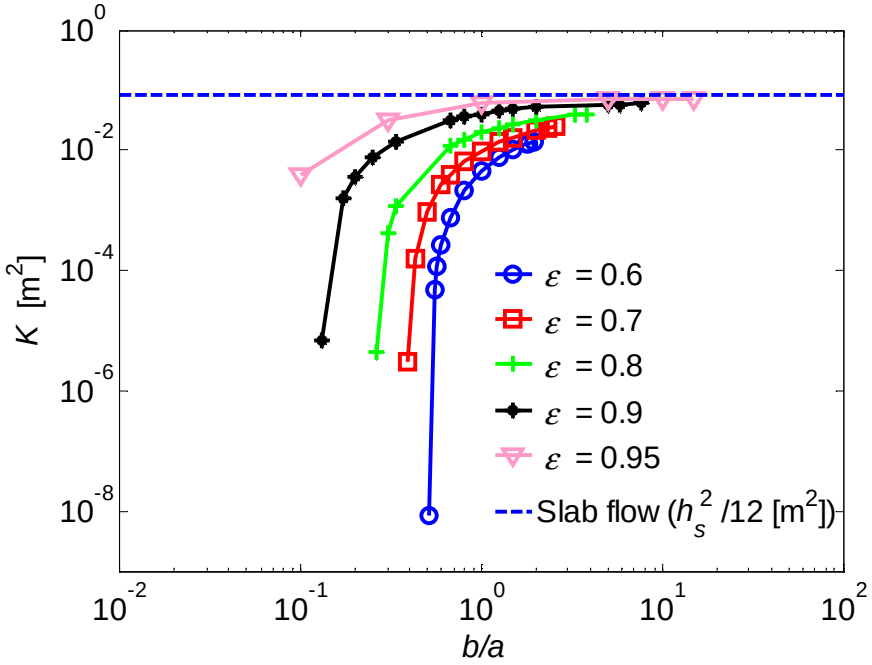

Figure 4: Effect of aspect ratio on the permeability of square configurations of ellipses with different porosities as given in the inset. The lines are only connecting the data-points as a guide to the eye.

2.5. Effect of orientation on the permeability of regular arrays

By changing the orientation (θ), i.e., the angle between the major axis of the obstacle and the horizontal axis, not only the values of the permeability tensor will change, but also its anisotropy will show up (so that the pressure gradient and the flow velocity are not parallel anymore). Therefore, the geometry of the pore structure has great effect on the permeability in irregular fibrous media. This effect for squares and ellipses (a/b = 2) is shown in Fig. 5.

For square shapes, at high porosities, the orientation does not much affect the permeability, whereas at low porosities the permeability depends a lot on the orientation. At θ = 45^0 we observe a drop in permeability, because we are close to the blocking situation, i.e., zero permeability, at a critical porosity (at which the permeability drops to zero) of $\varepsilon_c = 1 - \frac{1}{2\sin^2(45+\theta)} = 0.5$.

For ellipses, at high porosity, the orientation does not affect the permeability, whereas at low porosities the effect is strong. By increasing the orientation angle, i.e., by turning the major axis from horizontal to vertical, the permeability is reduced. The critical porosity $\varepsilon_c \approx 0.6073$ is purely determined by the major axis of the ellipse for $\theta = 90^0$.

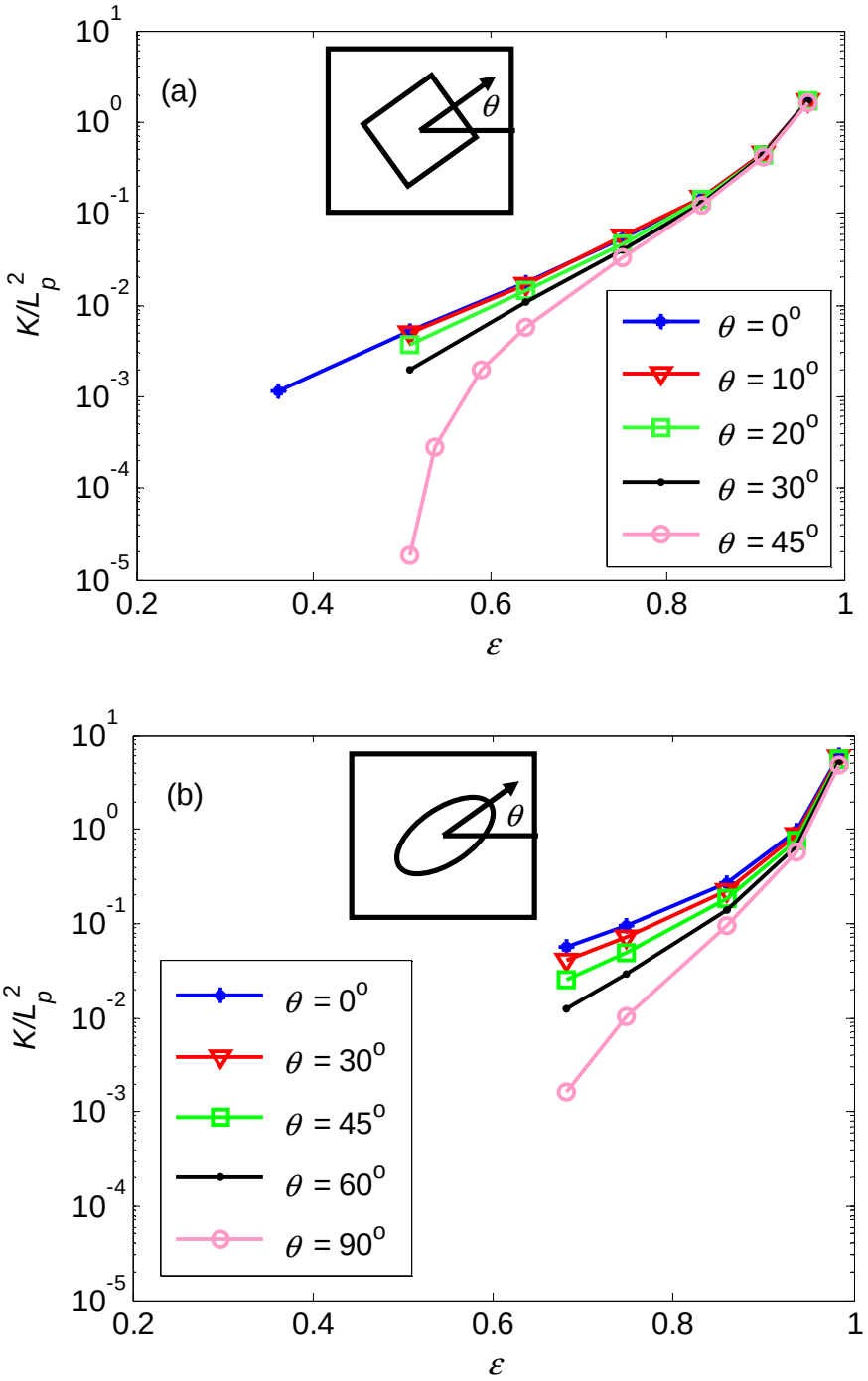

Figure 5: Effect of orientation (θ) on the normalized permeability for (a) square and (b) ellipse (a/b=2) in square packing configurations at different porosity. The lines are only connecting the data-points as a guide to the eye.

The general form of Darcy's law for anisotropic media in 2D in matrix form can be written as

$$\begin{Bmatrix} \langle U_x \rangle \\ \langle U_y \rangle \end{Bmatrix} = -\frac{1}{\mu}\begin{bmatrix} K_{11} & K_{12} \\ K_{21} & K_{22} \end{bmatrix}\begin{Bmatrix} \frac{\partial p}{\partial x} \\ \frac{\partial p}{\partial y} \end{Bmatrix} , \tag{8}$$

where $<U_x>$ and $<U_y>$ are superficial velocities in x and y direction, respectively. Then the permeability tensor for any value of θ can be calculated as

$$K_\theta = \begin{bmatrix} K_{11} & K_{12} \\ K_{21} & K_{22} \end{bmatrix} = R^T \begin{bmatrix} K_0 & 0 \\ 0 & K_{90} \end{bmatrix} R \tag{9}$$

where K_0 and K_{90} are the principal values of permeability that are determined from the values of $\theta = 0^0$ and $\theta = 90^0$, respectively. In Eq. (9), R^T is the transposed of the rotation matrix R, defined as (counterclockwise rotation by θ)

$$R = \begin{bmatrix} \cos(\theta) & -\sin(\theta) \\ \sin(\theta) & \cos(\theta) \end{bmatrix} \tag{10}$$

Eq. (9) shows that for $\theta \neq 0^0,\ 90^0$, one has $K_{12} \neq 0$, which means that by applying a pressure gradient in x direction, one gets a superficial velocity in y direction (i.e. anisotropic behavior because of oriented shape). Our numerical results are in good agreement with theoretical predictions (Eq. (9)) especially at high porosities (see the solid lines in Fig. 6). We have more deviation at low porosities (maximum discrepancy ≈ 5%) because of channel blockage and changes in flow behavior (the comparison is not shown here).

In Fig. 6, the variation of normalized permeability is shown as a function of the orientation angle θ. The normalized permeability is symmetric to 90^0 and decreases by increasing the orientation angle from 0^0. The eigenvalues of the permeability tensor are the extrema of the curves and the other data are well fitted by $K/L_p^2 = (K_0 + K_{90})/2 + (K_0 - K_{90})\cos(2\theta)/2$. By decreasing the aspect ratio a/b, we approach the value for the circular (cylinder) obstacle, i.e., a/b =1. The normalized permeability is symmetric to 45^0 for square shapes.

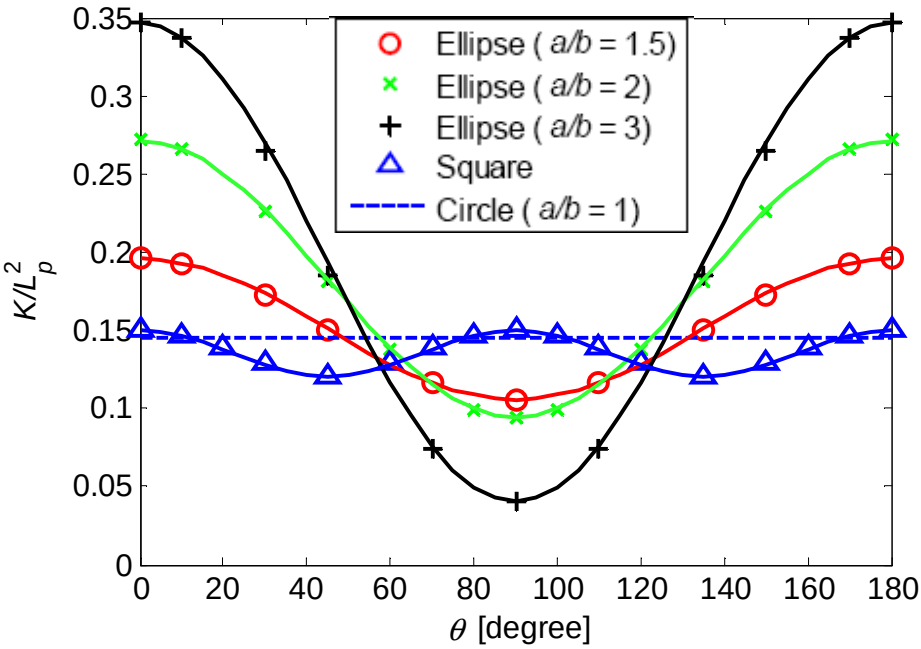

Figure 6: Normalized permeability plotted against orientation angle for different shapes at porosity $\varepsilon = 0.85$, for different obstacle shapes in square configurations. The dashed line represents circles. The solid lines show the theoretical predictions according to Eq. (9), where the eigenvalues are taken from the 0^0, 90^0 and 0^0, 45^0 degrees for ellipses and squares simulations, respectively.

2.6. Effects of staggered cell angle

In this subsection, the effect of another micro-structural parameter, the staggered cell angle, α, on the normalized permeability for circles (L_p=d) is discussed. The staggered angle is defined between the diagonal of the unit-cell and flow-direction (horizontal), see Fig. 7. In addition to the special cases $\alpha = 45^o$ and $\alpha = 60^o$, i.e., square and hexagonal packings, respectively, several other angles are studied. The contour of the horizontal velocity field component, for different α, at constant porosity $\varepsilon = 0.7$, is shown in Fig. 7. By changing α, the flow path and also the channel length will change. At $\alpha = 70^0$ and higher, the flow mainly follows a straight line, indicated by arrows in Fig. 7(a), with large superficial velocity and consequently large values of permeability. However, by decreasing α down to 35^0, the flow pattern completely changes and the superficial

velocity reduces, which should lead to lower and lower permeability. In brief, with increasing angle, both the superficial velocity and the permeability increase, with a plateau around $\alpha = 45^{o}$.

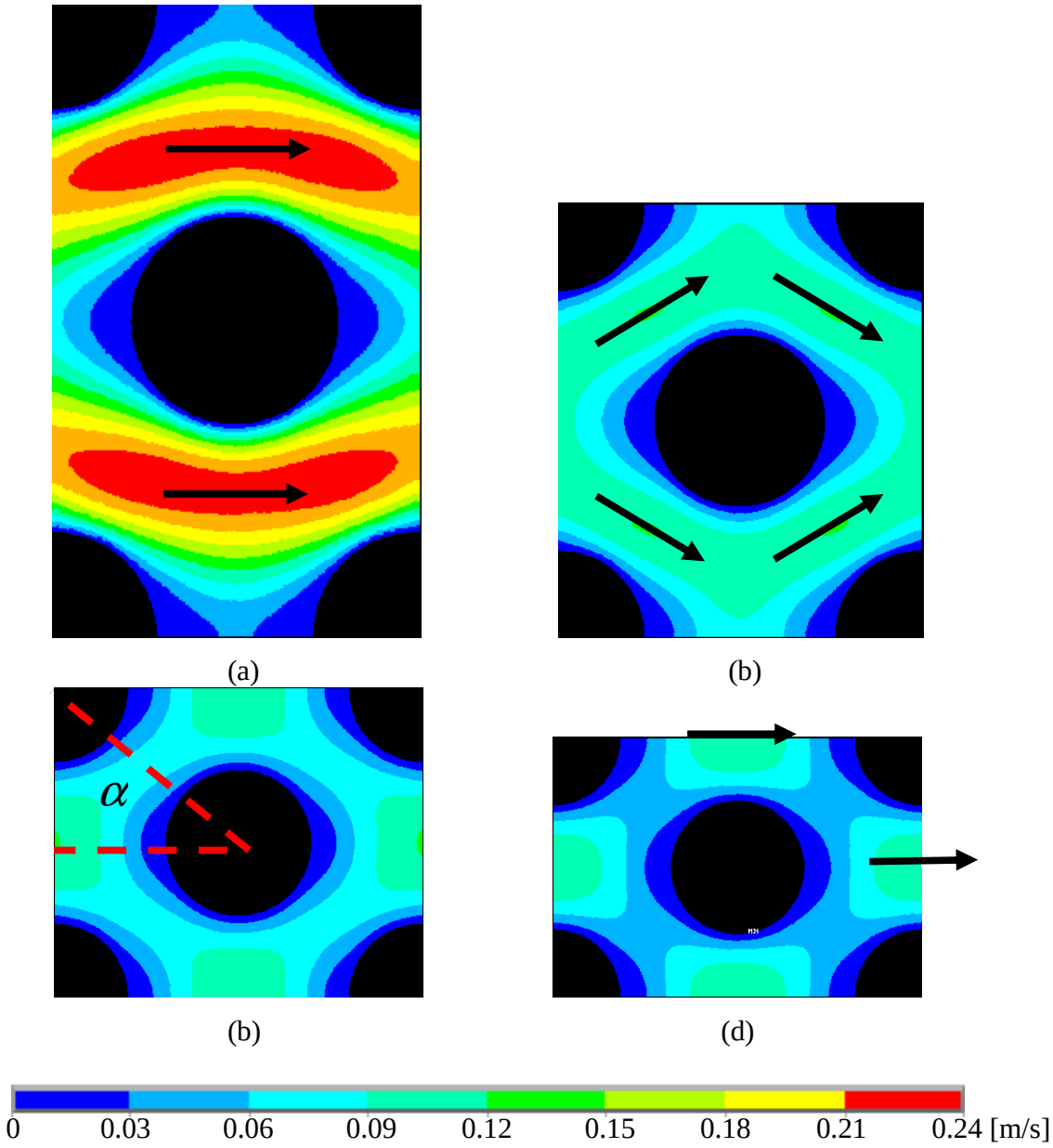

Figure 7: Horizontal velocity field components for (a) $\alpha = 60^{0}$, (b) $\alpha = 50^{0}$, (c) $\alpha = 40^{0}$ and (d) $\alpha = 35^{0}$ at fixed porosity $\varepsilon = 0.7$. The arrows indicate the main flow channel in (a) and (b). The staggered angle is defined between the diagonal of the unit-

cell and flow-direction (horizontal). The minimal angle $\alpha_{\min} = \tan^{-1}\left(\frac{2(1-\varepsilon)}{\pi}\right) = 10.81^0$ is realized when the vertical opening is closed, while the maximal angle $\alpha_{\max} = \tan^{-1}\left(\frac{\pi}{2(1-\varepsilon)}\right) = 79.18^0$ corresponds to the closed horizontal pore.

In Fig. 8 the normalized permeability is shown as function of the staggered angle, α, at different porosities. As it is seen the arrangement of particles relative to the flow direction is important in determining the permeability. By increasing α, the normalized permeability increases (the vertical distance between particles increases and therefore the resistance to the flow decreases) until it reaches a local maximum at $\alpha \cong 35^0$ – consistently for different porosities. At larger angles, it slightly decreases and attains a local minimum at $\alpha \cong 55^0$, beyond which it increases rapidly again. This behavior can be explained by the variation of the area-fraction distribution with α on the planes perpendicular to the flow direction, as discussed by Alcocer et al. (1999).

The normalized permeability as a function of α can be expressed as a cubic polynomial

$$\frac{K}{d^2} = \mathrm{A}\left(\frac{\alpha - 45^0}{45^0}\right)^3 + \mathrm{B}\left(\frac{\alpha - 45^0}{45^0}\right)^2 + \mathrm{C}\left(\frac{\alpha - 45^0}{45^0}\right) + \mathrm{D} \qquad (11)$$

where A, B, C and D are dimensionless constants, listed in Table 2 for different porosities.

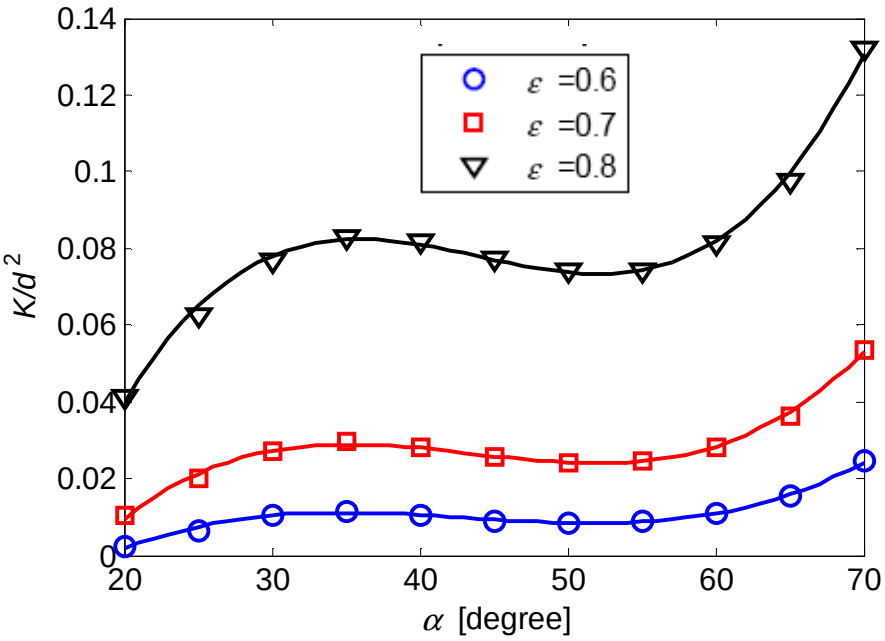

Figure 8: The variation of normalized permeability versus staggered unit cell angle α at different porosities, as given in the inset. The solid lines show the fit (Eq. (11))

Table 2: Fitted parameters for the permeability-staggered angle relation

	$\varepsilon = 0.8$	$\varepsilon = 0.7$	$\varepsilon = 0.6$
A	0.38401	0.18813	0.09913
B	0.02682	0.01738	0.01171
C	-0.03693	-0.01914	-0.01027
D	0.07698	0.02584	0.009319

The leading term with A is dominating, the term with B is a rather small correction, the term with C sets the (negative) slope in the center, and the term with D determines the offset. All fit-parameters depend on porosity and it should be noted that the range of available angles is limited and also depends on porosity. Additional scaling- and fit-attempts (data not shown) did not lead to much better results, thus we only present this empirical fit here.

The decreasing region, i.e., $35^0 \le \alpha \le 55^0$ corresponds to the case in which the flow goes in a preferred channel orthogonal/perpendicular to the line (diagonal) connecting two particles, see Figs. 7(b) and (c). While in cases with larger α, the flow goes at straight

lines/channels, see Fig. 7(a), the configuration for smaller α is dominated by the narrow vertical opening between two obstacles. In essence, in the plateau region, the permeability is not much affected by the staggered angle α. This observation might be useful during design and manufacturing of fibrous composites.

In summary, the results of this section show that the macroscopic permeability not only depends on the porosity but also on the microstructure, namely shape, aspect ratio and orientation of particles.

3. Theoretical prediction of the permeability for all porosities

In this section, based on the observations in the previous section, and using the velocity profiles from FE unit cell simulations, a generalized form of the Carman Kozeny (CK) equation for the permeability of fibrous porous media (2D regular arrays of particles) is proposed.

3.1 From special cases to a more general CK equation

The earliest and most widely applied approach in the porous media literature, for predicting the permeability, involves capillary models (Carman 1937) such as the one that leads to the CK equation. The approach to obtain this equation is based on Poiseuille flow through pipes. Assuming pipe flow through a cylindrical channel of diameter h_p, the average velocity through the channel is

$$\langle u_p \rangle = -\frac{h_p^2}{32\mu}\frac{\Delta p}{L} \quad , \tag{12}$$

and for slab flow through an infinite channel of width h_s

$$\langle u_s \rangle = -\frac{h_s^2}{12\mu}\frac{\Delta p}{L} \quad , \tag{13}$$

given the pressure drop Δp per length L, and a fluid with viscosity μ.

Defining the hydraulic diameter

$$D_h = 4\frac{\text{volume available for flow}}{\text{total wetted surface}} \quad , \tag{14}$$

allows to unify the relations above, by combining Eq. (14) with either Eq. (12), with $D_h = h_p$, or Eq. (13), with $D_h = 2h_s$, and with Darcy's law, Eq. (2), so that the permeability is described by the CK relation (Carman 1937)

$$K = \frac{\varepsilon \mu \langle u \rangle}{\nabla p} = \frac{\varepsilon D_h^2}{\psi_{CK}} \tag{15}$$

Where, ψ_{CK} =32 (or 48) is the dimensionless Kozeny factor, characteristic of the pipe (or slab) pore structure. When one has obstacles like fibers (or particles) instead of straight pores, the hydraulic diameter can be re-written as

$$D_h = \frac{4\varepsilon V}{S_v} = \frac{4\varepsilon}{(1-\varepsilon)a_v} = \frac{\varepsilon d}{(1-\varepsilon)}, \quad \text{with } a_v = \frac{\text{particle surface}}{\text{particle volume}} = \frac{S_v}{(1-\varepsilon)V} = \frac{4}{d} \quad , \tag{16}$$

with the total volume of the unit cell, V, the total wetted surface, S_v, the specific surface area, a_v, and the porosity, ε, for a fibrous medium of fiber diameter d. Note that the hydraulic diameter, in this way, is expressed as a function of the measurable quantities porosity and specific surface area. The above value of a_v is for circles (cylinders) – for spheres one has a_v=6/d. In this formulation, we just consider the resistance due to presence of particles (no slip boundaries at the surface of the particles) and neglect the outer walls.

Inserting Eq. (16) into Eq. (15), yields the normalized permeability for fibers

$$\frac{K}{d^2} = \frac{1}{\psi_{CK}} \frac{\varepsilon^3}{(1-\varepsilon)^2} \quad , \tag{17}$$

which depends non-linearly on the porosity and on a shape/structure factor, ψ_{CK}.

One of the main drawbacks of the CK equation is that the Kozeny factor ψ_{CK} is a-priori unknown in realistic systems and has to be determined experimentally. An ample amount of literature exists on the experimental and theoretical determination of the Kozeny factor, but we are not aware of a theory that relates ψ_{CK} with the microstructure, i.e., the porosity, the random configuration, tortuosity, and other microscopic quantities. An overview of experimental and theoretical approaches can be found in Astroem et al. (1992), which mainly deals with fibrous media, and Torquato (1991), which is based on variational principles. One of the most widely accepted approaches to generalize the CK

relation was proposed by Carman (1937), who noticed that the streamlines in a porous medium are far from being completely straight and parallel to each other. This effect can be described by a dimensionless parameter, L_e/L (tortuosity), with the length of the streamlines, L_e, relative to the length of the sample, L. Hence the Kozeny factor can be split into

$$\psi_{CK} = \Phi\left(\frac{L_e}{L}\right)^2 \tag{18}$$

where Φ is the effect of particle shape, which can be seen as a fitting parameter. In fact, the tortuosity and the shape factor reflect the effects of microstructure on the macroscopic properties (like permeability) of the porous media.

In the original form of the CK equation for random 3D sphere structures, it is assumed that the tortuosity is a constant for all ranges of porosities and is equal to $\sqrt{2}$ and the fitting parameter, Φ, then becomes 90 for the case of pipe flow and 60 for slab flow.

Knowing the values of the normalized permeability from our FE simulations, we can compare the values of the Kozeny factor based on our numerical results and available theoretical data and with the original ψ_{CK} =120 for slab flow, see Eqs. (17) and (18). The comparison is shown in Fig. 9. At a certain range of porosities, $0.5 < \varepsilon < 0.7$, the CK factor ψ_{CK} is indeed not varying much. However, at higher or lower porosities, it strongly depends on porosity and structure. At high and low porosities, our numerical results are in good agreement with the predictions of Drummond et al. (1984) and Gebart (1992), respectively (see Table 1). These results indicate that the Carman-Kozeny factor, ψ_{CK}, is indeed not constant and depends on the microstructure.

In the following subsections, we will study the dependency of ψ_{CK} on the micro-structural parameters.

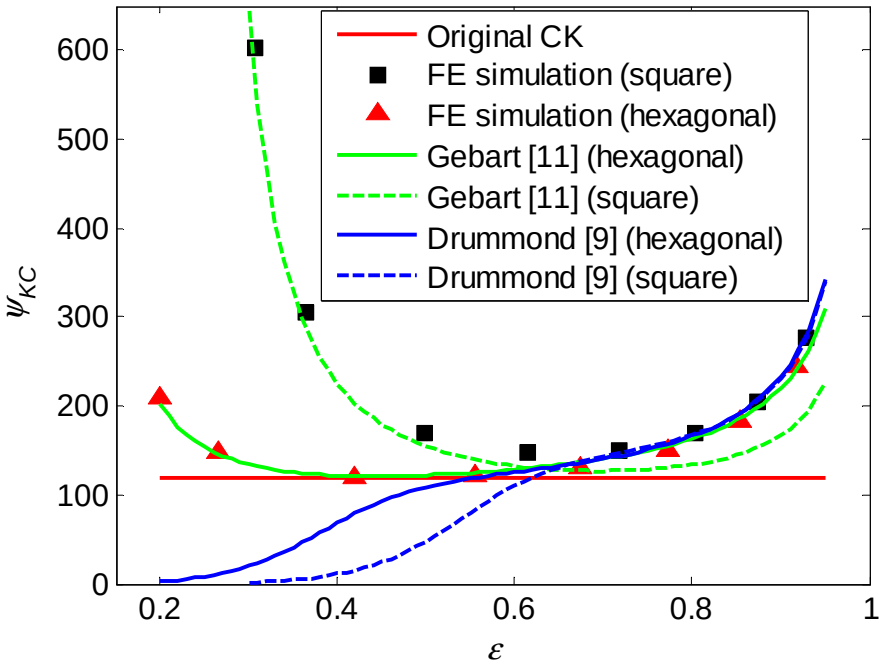

Figure 9: Kozeny factor plotted as a function of porosity for different models (lines) and data sets (symbols) as given in the inset.

3.2. Measurement of the tortuosity (L_e/L)

As discussed before, the tortuosity is the average effective streamline length scaled by system length, L_e/L, and one possible key parameters in the Kozeny factor in the CK equation (Carman 1937). From our numerical simulations, we extract the average length of several streamlines (using 8 streamlines that divide the total mass in-flux into 9 zones, thus avoiding the center and the edges). By taking the average length of these lines, the tortuosity can be obtained, while by taking the standard deviation of the set of streamlines, the homogeneity of the flow can be judged. The tortuosity is plotted in Fig. 10 as function of porosity for different shapes and orientations and as function of the staggered angle α for different porosities.

Unlike the traditional form of the CK equation, which assumes that $L_e / L = \sqrt{2}$ (for random 3D structures) is constant (Carman 1937), our numerical results show that the tortuosity (i) is smaller and (ii) depends on the porosity and the pore structure. In Fig.10(a), as intuition suggests, the vertical and horizontal ellipses have the highest and

lowest average tortuosity, respectively. This goes ahead with very large and very small standard deviation, i.e., the vertical ellipse configuration involves the widest spread of streamline lengths. In the case of a circular shape obstacle, the (average) tortuosity is between the horizontal and vertical ellipse cases and, for intermediate porosity, becomes almost independent of porosity, with constant standard deviation that is wider than the average tortuosity deviation from unity. The square shape obstacles are intermediate in tortuosity, i.e., the 0^0-square (45^0-square) shapes take tortuosity values between the horizontal (vertical) ellipse and the circular obstacles.

In Fig. 10(b), the tortuosity is plotted against the staggered unit cell angle α. By increasing α the value of tortuosity increases until about $\alpha \cong 45^0$, where it reaches its maximum. Note that the standard deviation remains small for all angles smaller than $\alpha \cong 45^0$. At higher angles, tortuosity decreases, while its standard deviation considerably increases. At large values of α, most of the fluid flow goes along a straight line, however, near the boundary, we have a few longer streamlines that cause the large standard deviation. At the limit case of $\alpha \approx \alpha_{\max}$, when the upper particles touch, see Fig. 7, the tortuosity approaches unity (data not shown) and the flow goes mostly along a straight channels.

3.3. Measurement of the shape/fitting factor (Φ)

Knowing the values of tortuosity, L_e/L, and normalized permeability, K/d^2, from our FE simulations, we can obtain the values of Φ for different shapes and orientations as $\Phi = \psi_{CK} \Big/ \left(\frac{L_e}{L} \right)^2$. In Fig. 11 the variation of Φ as a function of porosity for different shapes and orientations is shown. Unlike the traditional CK factor, the shape/fitting factor is not only a function of porosity but also depends on the orientation of particles/cylinders. This dependency is more pronounced at high (low) porosities and close to the blocking conditions, i.e., ellipses with 90^0 and squares with 45^0.

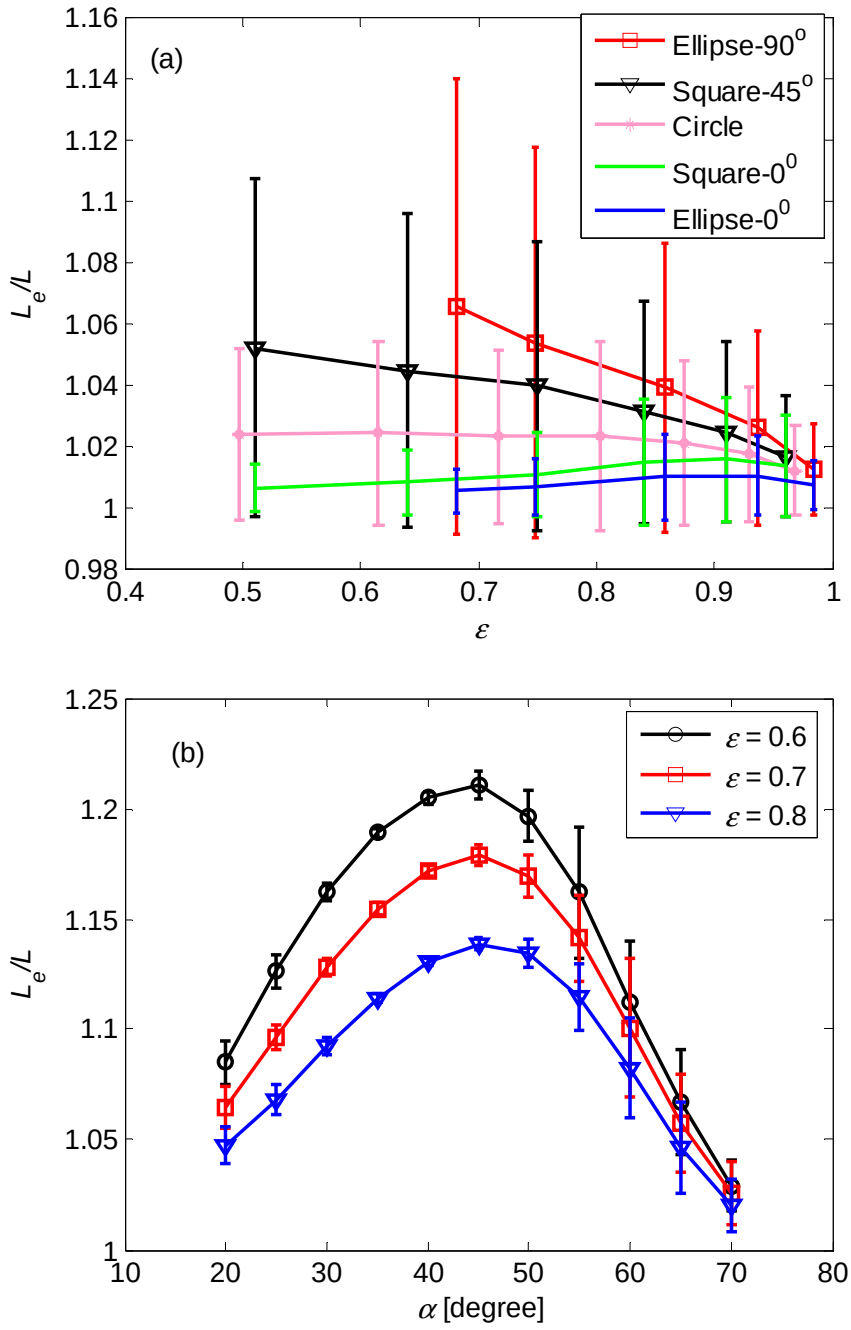

Figure 10: Tortuosity (L_e / L) (a) plotted as a function of porosity for different obstacle shapes and orientations on square configurations, $\alpha = 45^o$, (b) plotted as a function of the staggered cell angle, α, as given in the inset, for circles at different porosities on hexagonal configurations. Error bars give the standard deviation of the 8 streamline

lengths, where bottom-values below unity indicate a highly non-symmetric distribution around the average.

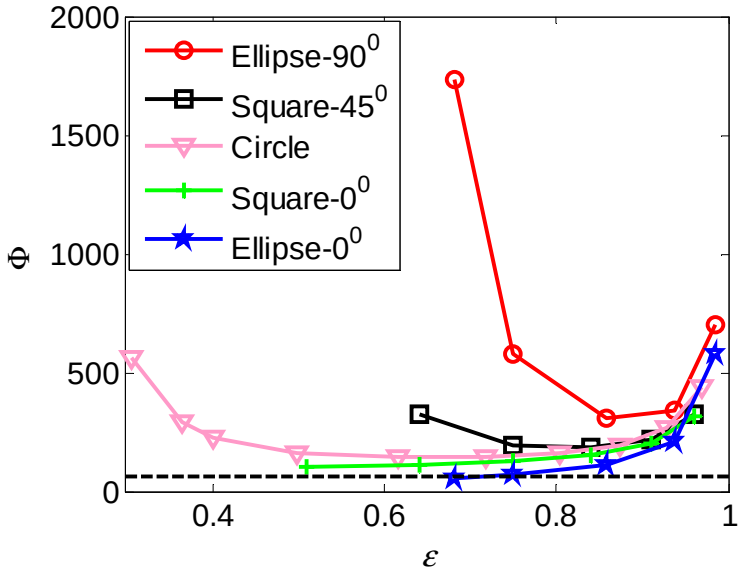

Figure 11: Shape/fitting factor, Φ, plotted as a function of porosity for different obstacle shapes and orientations on square configurations, $\alpha = 45^{o}$. The straight dashed line shows the value of $\Phi = 60$ as in the original CK factor.

3.4. Corrections to the limit theories

Being unable to explain the variation of permeability with tortuosity and a constant shape factor, now we attempt to optimize/correct the limit theories by Gebart (1992) and Drummond et al. (1984), see Table 1, in order to propose an analytical relation for the permeability that is valid for all porosities and for square and hexagonal arrays of cylinders.

3.4.1 Square configuration

Assuming one particle at the center, pressure boundary at the left and right and periodic top and bottom, we correct the original Gebart relation from Table 1, K_G^s, by a linear correction term $K_{G2}^s = K_G^s \dfrac{1}{1+g_2\left(\varepsilon-\varepsilon_c\right)}$, with g_2=0.336. After observation of a linear

correction term in the denominator, the linear least square method is used to get the coefficient g_2. In contrast to K_G^s, which asymptotically approaches the limit case, $\varepsilon \to \varepsilon_c$, but for $\varepsilon \approx 0.6$ deviates already by about 10%, the correction, K_{G2}, has a maximum discrepancy in the range $\varepsilon_c < \varepsilon < 0.85$ of less than 10%, and for $\varepsilon_c < \varepsilon < 0.7$ of less than 2%, see the squares in Fig. 12.

Since the Drummond relation from Table 1, K_D^s, is valid at high porosities with maximum discrepancy at $0.7 < \varepsilon < 1$ of less than 10% and for $0.8 < \varepsilon < 1$ of less than 2%, we propose the following merged function

$$K^s = K_{G2}^s + \left(K_D^s - K_{G2}^s\right) m(\varepsilon), \text{ with } m(\varepsilon) = \frac{1 + \tanh\left(\left(\varepsilon - \varepsilon_h\right)/\varepsilon_t\right)}{2}, \quad \varepsilon_h = 0.75, \quad \varepsilon_t = 0.037,$$

that is valid for the whole range of porosity, with deviations of less than 2% that also includes the analytical relations for the limit cases. While the choice of *m(ε)* is arbitary, the non-linear least square fitting procedure is used to obtain the empirical coefficients ε_h and ε_t. The error of these coefficients is defined by their standard deviation.

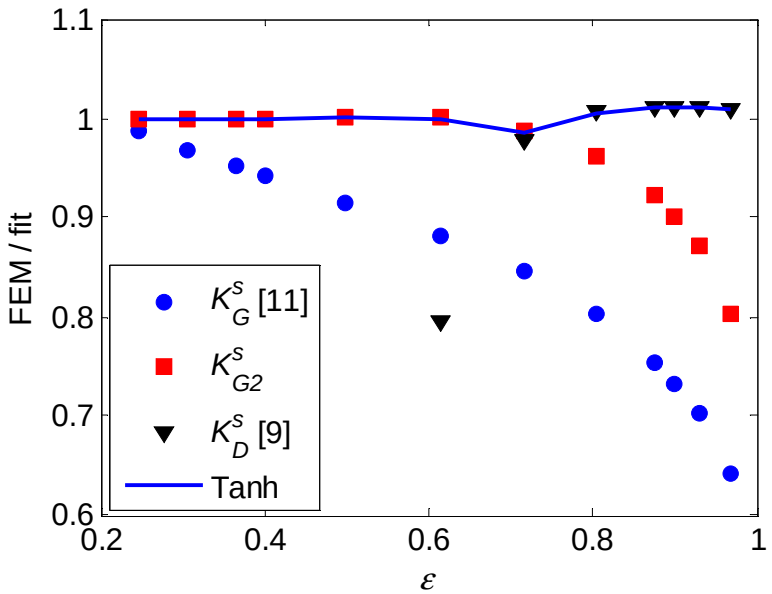

Figure12: Relative error between FEM results and proposed corrections for square configuration with the critical porosity $\varepsilon_c = 1 - \pi/4$.

3.4.2 Staggered hexagonal configuration $\alpha = 60^0$:

In this situation, the correction to the Drummond relation from Table 1 is $K^h_{D2} = d_1 K^h_D \left(1 + d_2 \varepsilon\right)$, $K^h = K^h_G + \left(K^h_{D2} - K^h_G\right) m\left(\varepsilon\right)$, with d_1=0.942, d_2=0.153, $\varepsilon_h = 0.55$, $\varepsilon_t = 0.037$, leads to a corrected permeability for all porosities, with a maximum error of less than 2%, see Fig. 13.

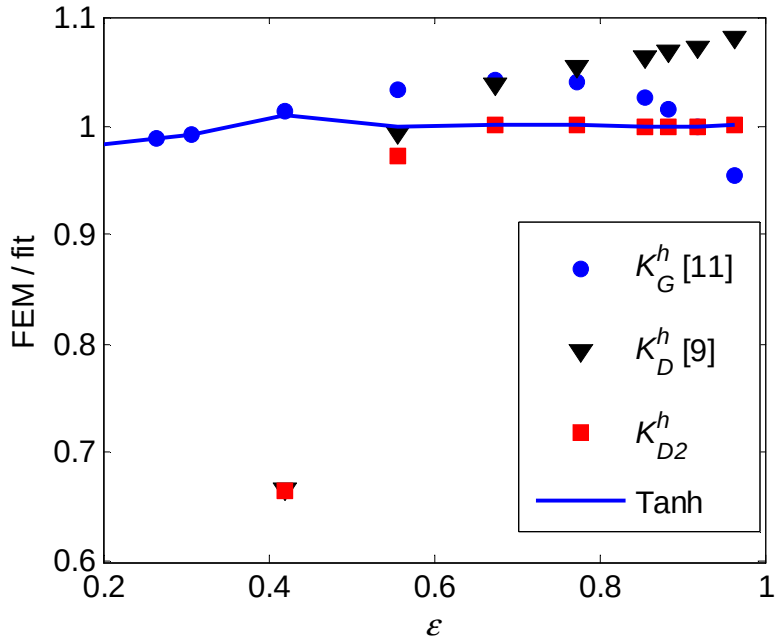

Figure 13: Relative error between FEM results and proposed fits for hexagonal configuration with the critical porosity $\varepsilon_c = 1 - \pi / \left(2\sqrt{3}\right)$.

4. Summary and Conclusions

The permeability of porous structures is an important property that characterizes the transport properties of porous media; however, its determination is challenging due to its complex dependence on the microstructure of the media. Using an appropriate representative volume element, transverse flow in aligned, periodic fibrous porous media has been investigated based on high resolution (fine grid) FE simulations. This is

complementary to previous studies by Hill et al. (2001) and Van der Hoef et al. (2005) who obtained the drag/permeability relation for random arrays of mono- and bi-disperse spheres at low and moderate Reynolds numbers. In all of our simulations, the total pressure drop has been chosen small, such that we are always in Darcy's regime (creeping flow). In particular, the effects of different parameters including fiber (particle) shape, aspect ratio, orientation, and staggered unit cell angle on the normalized permeability are measured and discussed in detail for the full range of porosities. The conclusions are:

- The present results for the permeability are validated by comparing with available theoretical and numerical data for square and hexagonal arrays over a wide range of porosities. Especially in the limits of high and low porosity, agreement with previous theoretical results is established.
- By increasing the staggered unit cell angle, α (where 60 degrees corresponds to the hexagonal array), from the blocked configuration with minimal angle $\alpha_{\min}$, the normalized permeability increases until it reaches its local maximum at $\alpha \cong 35^0$. Then it decreases a bit (almost plateau) until it reaches its local minimum at $\alpha \cong 55^0$. From there it increases again until a maximum porosity is reached at $\alpha_{\max}$. The best-fit (3^{rd} order) polynomials at different porosities are presented as reference for later use.
- By increasing the orientation angle of the ellipses (here the longer axis of ellipses was used to define the orientation relative to the flow direction), the permeability decreases and shows its anisotropy. The permeability values for the extreme cases, i.e., eigenvalues at 0^0 and 90^0, are used to predict the permeability for arbitrary orientation angles, see Eq. (9).
- By increasing the aspect ratio of horizontal ellipses, the permeability increases and approaches the permeability of slab flow, i.e., $K = h_s^2/12 = 0.0833$ [m^2] at high porosities.
- Using the hydraulic diameter concept the permeability can be expressed in the general form of the (Carman-Kozeny) CK equation. Our numerical results show that the CK factor not only depends on the porosity but also on the pore structure, namely particle shape, orientation and staggered angle α.
- The numerical results show that immobile circles and ellipses have the lowest and highest permeability, respectively. The relevance of this observation for flows of gas/fluid-solid with moving non-spherical particles is an open question.

Since analytical forms with the power as a free fit-parameter are neither consistent with the highest porosity asymptote, nor with the lowest porosity limit case, those fits are only an attempt to describe the intermediate regime of practical importance with a closed functional form. In order to improve the analytical relation for the permeability, to be applied, e.g., for DEM-FEM coupling, we proposed a merged function that includes both limit cases of low and high porosity and is smooth in between with maximal deviation from our numerical results of less than 2%.

Future work will investigate the creep and inertial flow regime through periodic and disordered arrays, the relation between microstructure and (macro) permeability, and the effect of the size of the system, especially for random/disordered structures. Since already the packing generation algorithm affects the permeability in random arrays of parallel cylinders, different procedures have to be compared and evaluated with respect to the microstructure. These results can then be utilized for validation of advanced, more coarse-grained models for particle-fluid interaction and their coupling-terms between the discrete element method (DEM) for the particles and the FEM or CFD solver for the fluid, in a multi-scale coarse grained approach.

Acknowledgements:

The authors thank N. P. Kruyt, A. Thornton and T. Weinhart for helpful discussion and acknowledge the financial support of STW through the STW-MuST program, project number 10120.

References

[1] Alcocer, F.J., Kumar, V. and Singh, P., 1999. Permeability of periodic porous media, Physical Review E 59(1), 711-14.

[2] Astroem, B., Pipes, R., Advani, S., 1992. On flow through aligned fiber beds and its application to composite processing, Journal of Composite Materials 26 (9), 1351– 73.

[3] Berryman, J.G., Wang, H.F., 2000. Elastic wave propagation and attenuation in a double-porosity dual-permeability medium, International Journal of Rock Mechanics and Mining Sciences 37, 63-78.

[4] Bird, R.B., Stewart, W.E. and Lightfoot, E.N., 2001. Transport Phenomena, 2nd edn,. John Wiley & Sons.

[5] Bruschke, M.V. and Advani, S.G., 1993. Flow of generalized Newtonian fluids across a periodic array of cylinders, Journal of Rheology 37, 479-98.

[6] Carman, P.C., 1937. Fluid flow through granular beds, Transactions of the Institute of Chemical Engineering 15, 150–166.

[7] Chen, X., Papathanasiou, T.D., 2008. The transverse permeability of disordered fiber arrays: A statistical correlation in terms of the mean nearest interfiber spacing, Transport in Porous Media 71 (2), 233-251.

[8] Crawford, J.W., Matsui, N., Young, I.M., 1995. The relation between the moisture-release curve and the structure of soil, Euro J. Soil Sci. 46, 369-375.

[9] Drummond, J.E. and Tahir, M.I., 1984. Laminar viscous flow through regular arrays of parallel solid cylinders, Int. J. Multiphase Flow 10, 515-40.

[10] Dullien, F.A.L., 1992. Porous Media: Fluid Transport and Pore Structure, 2nd edn. Academic Press, New York.

[11] Gebart, B.R., 1992. Permeability of Unidirectional Reinforcements for RTM, Journal of Composite Materials 26, 1100–33.

[12] Happel, J., 1959. Viscous flow relative to arrays of cylinders, AIChE 5, 174– 7.

[13] Hasimoto, H., 1959. On the periodic fundamental solutions of the Stokes equations and their application to viscous flow past a cubic array of spheres, J. Fluid Mech. 5, 317–328.

[14] Hilfer, R., 2000. Local porosity theory and stochastic reconstruction for porous media, in: K. Mecke and D. Stoyan (eds.), Statistical Physics and Spatial Statistics, Lecture Notes in Physics, Springer, Berlin.

[15] Hill, R.J., Koch, D.L. and Ladd, A.J.C., 2001. Moderate-Reynolds-number flows in ordered and random arrays of spheres, Journal of Fluid Mechanics 448, 243-278.

[16] Hill, R.J., Koch, D.L. and Ladd, A.J.C., 2001. The first effects of fluid inertia on flows in ordered and random arrays of spheres, Journal of Fluid Mechanics 448, 213-241.

[17] Jackson, G.W., James, D.F., 1986. The permeability of fibrous porous media, Can. J. Chem. Eng. 64, 364–374.

[18] Koch, D.L., Ladd, A.J.C., 1997. Moderate Reynolds number flows through periodic and random arrays of aligned cylinders, Journal of Fluid Mechanics 349, 31–66.

[19] Kuipers, J.A.M., Van Duin, K.J., Van Beckum, F.P.H., Van Swaaij, W.P.M., 1993. Computer simulation of the hydrodynamics of a two-dimensional gas-fluidized bed, Computers Chem. Eng. 17, 839-858.

[20] Kuwabara, S., 1959. The forces experienced by randomly distributed parallel circular cylinders or spheres in a viscous flow at small Reynolds numbers, Journal of the Physical Society of Japan 14, 527–532.

[21] Lee, S.L., Yang, J.H., 1997. Modeling of Darcy–Forchheimer drag for fluid flow across a bank of circular cylinders, Int. J. Heat Mass Transfer 40, 3149–55.

[22] Laakkonen, K., 2003. Method to model dryer fabrics in paper machine scale using small scale simulations and porous media model, Int. J. Heat Fluid Flow 24, 114–121.

[23] Moss, G.R., Rothstein, J.P., 2010. Flow of wormlike micelle solutions through a periodic array of cylinders, Journal of Non-Newtonian Fluid Mechanics 165 (1-2), 1-13.

[24] Muller, A.J. and Saez, A.E., 1999. The Rheology of Polymer Solutions in Porous Media, Flexible Polymer Chains in Elongational Flow, Theories and Experiments, Springer-Verlag, Heidelberg.

[25] Obdam, A.N.M., Veling, E.J.M., 1987. Elliptical inhomogeneities in groundwater flow-An analytical description, Journal of Hydrology 95, 87–96.

[26] Roth, K., 2008. Scaling of water flow through porous media and soils, Euro. J. Soil Sci. 59 (1), 125-130.

[27] Sahraoui, M., Kaviany, M., 1992. Slip and no-slip boundary conditions at interface of porous, plain media, Int. J. Heat Mass Transfer 35, 927–43.

[28] Sangani, A.S., Acrivos, A., 1982. Slow flow past periodic arrays of cylinders with application to heat transfer, Int. J. Multiphase Flow 8, 193–206.

[29] Shani, C., Weisbrod, N., Yakirevich, A., 2008. Colloid transport through saturated sand columns: Influence of physical and chemical surface properties on deposition, Colloids and Surfaces A: Physicochemical and Engineering Aspects 316 (1-3), 142-150.

[30] Sorbie, K.S., Parker, A., Clifford, P.J., 1987. Experimental and theoretical study of polymer flow in porous media, SPE Reservoir Eng. 2, 281-304.

[31] Sullivan, R.R., 1942. Specific surface measurements on compact bundles of parallel fibers, J. Appl. Phys. 13, 725–730.

[32] Torquato S., 1991. Random heterogeneous media: Microstructure and improved bounds on effective properties, Appl. Mech. Rev. 44, 37-77.

[33] Van der Hoef, M.A., Beetstra, R., Kuipers, J.A.M., 2005. Lattice-Boltzmann simulations of low-Reynolds-number flow past mono- and bidisperse arrays of spheres: Results for the permeability and drag force, Journal of Fluid Mechanics 528, 233-254.

[34] Wallstrom, T.C., Christie, M.A., Durlofsky L.J., Sharp D.H., 2002. Effective flux boundary conditions for upscaling porous media equations, Transport in Porous Media 46, 139–153.

[35] Wang, C.Y., 2002. Slow Viscous Flow between Hexagonal Cylinders, Transport in Porous Media 47, 67–80.

[36] Wanner, O., Cunningham, A.B., Lundman, R., 1995. Modeling biofilm accumulation and mass transport in a porous medium under high substrate loading, Biotechnology and bioengineering 47, 703-712.

[37] Yazdchi, K., Srivastava, S. and Luding, S., 2010. On the transition from creeping to inertial flow in arrays of cylinders, Proceedings of IMECE, Vancouver, Canada, 6 pages, ISBN-978-0-7918-3891-4.

[38] Zhao, C., Hobbs, B.E., Ord, A., Peng, S., Liu, L., Mühlhaus H.B., 2006a. Analytical solutions for pore-fluid flow focusing within inclined elliptic inclusions in pore-fluid-saturated porous rocks: Solutions derived in an elliptical coordinate system. Mathematical Geology 38, 987–1010.

[39] Zhao, C., Hobbs, B.E., Ord, A., Peng, S., Liu, L., 2008. Inversely-Mapped Analytical Solutions for Flow Patterns around and within Inclined Elliptic Inclusions in Fluid-Saturated Rocks, Mathematical Geosciences 40, 179–197.

[40] Zimmerman, R.W., 1996. Effective conductivity of a two-dimensional medium containing elliptical inhomogeneities, Proceedings of the Royal Society A: Mathematical, Physical and Engineering Sciences 452, 1713–27.